



Hyperion

D6.1 Conceptual framework for remote sensing-based CH monitoring

Deliverable number	D6.1
Deliverable title	Conceptual framework for remote sensing-based CH monitoring
Nature ¹	R
Dissemination Level ²	PU
Authors (email) Institution	Karathanassi V. karathan@survey.ntua.gr , Georgopoulos A. drag@central.ntua.gr , Doulamis A. adoulam@cs.ntua.gr , NTUA Enriques Hernandez-Montes emontes@ugr.es UGR
Editor (email) Institution	Karathanassi V. karathan@survey.ntua.gr NTUA
Leading partner	NTUA
Participating partners	UGR, ICCS, INIPD
Official submission date:	31/03/2020
Actual submission date:	

¹ **R**=Document, report; **DEM**=Demonstrator, pilot, prototype; **DEC**=website, patent fillings, videos, etc.; **OTHER**=other

² **PU**=Public, **CO**=Confidential, only for members of the consortium (including the Commission Services), **CI**=Classified, as referred to in Commission Decision 2001/844/EC

Modifications Index	
Date	Version
26/2/2020	1.0 First version
	1.1 Quality Review



This work is a part of the HYPERION project. HYPERION has received funding from the European Union’s Horizon 2020 research and innovation programme under grant agreement no 821054.

Content reflects only the authors’ view and European Commission is not responsible for any use that may be made of the information it contains.

ACRONYMS AND ABBREVIATIONS

CH	Cultural Heritage
MSI	Multispectral images
GGS	Generic Ground Station
HCAA	Hellenic Civil Aviation Authority
SAR	Synthetic Aperture Radar
UAS	Unmanned Aircraft Systems
RS-MMS	Remote Sensing-based Multiscale Monitoring System
EMS	Emergency Management Service
HRAP	Holistic Resilience Assessment Platform
GCS	Ground Control Station
ATC	Air Traffic Control
MVS	Multi-View Stereo
SfM	Structure from Motion
TLS	Terrestrial Laser Scanning
ATC	Air Traffic Control

Table of Contents

1. Introduction	7
1.1 Background	7
1.2 Scope and Objective	7
2. The components of the RS-based multiscale monitoring system	8
2.1 The data acquisition/selection component.....	8
2.1.1 GCS deployment.....	8
2.1.2 Satellite images.....	10
2.2 The data processing component.....	13
2.2.1 The Ground Generic Station concept.....	13
2.2.2 3D representation methods.....	13
2.2.3 Satellite image processing methods.....	14
2.2.4 Hyperspectral methods.....	20
3. MMS products.....	22
3.1 3D representations	22
3.2 Satellite remote sensing-based maps.....	23
3.2.1 Ground displacement results.....	23
3.2.2 Earthquake and landslide results.....	24
3.2.3 Flood mapping results.....	26
3.2.4 Land cover change detection results.....	26
3.3 Copernicus EMS products.....	27
4. MMS operational functions.....	28
4.1 Routine monitoring.....	28
4.2 Post-disaster monitoring.....	28
5. Communication with HRAP.....	28
5.1 MMS product formats.....	28
5.1.1 Metadata.....	29
5.1.2 Use of Metadata in the context of the HYPERION project.....	30
5.2 MMS product repository.....	33
5.3 Dynamic link to hazard and resilience assessment.....	35
6. References.....	36

List of Figures

List of Tables

Executive Summary

This deliverable includes the description of the Remote Sensing-based Multiscale Monitoring System (RS-MMS). It describes the relevant system components, products, functionalities and communication links that will ensure connection with the HYPERION platform.

In chapter 2, data procurement and data processing, the main components of the RS-MMS, are described. Data procurement includes the Ground Control System that is responsible for ground and airborne image acquisition of the CH monuments. The document describes the GCS as well as the most appropriate satellite imagery for the monitoring of the pilot areas. Data processing will be carried out in the Generic Ground Station. In this deliverable, new state of the art methods are briefly described to document the main decisions on the advanced image processing and data analysis methods that will be developed and/or applied within the HYPERION framework.

The RS-MMS products are described in chapter 3. Some products, such as 3D representation of the monuments, land deformation, etc., address the needs of routine monitoring, while some others address post-disaster requirements and are generated after an earthquake, a flood event, etc. RS-MMS operational functions are described in chapter 4.

All the products are stored in the RS-MMS repository, which has the task to communicate with HRAP via the middleware. For this communication, appropriate metadata for the RS-MMS products will be created and an appropriate web cataloguing service for geospatial data (GeoNetwork) will be used. The technical specifications are described in chapter 5. Finally, the appropriate methods that will be developed for dynamic link to hazard and resilience assessment are reported in the same chapter.

The deliverable is intended for public use, and it will particularly be helpful for the partners involved in the design of the HYPERION platform.

1. Introduction

1.1 Background

The deliverable D6.1 “Conceptual framework for remote sensing-based CH monitoring” sets the baselines for the development and operation of the remote sensing-based multiscale monitoring system. RS-MMS is one of the basic milestones of the Hyperion project since it provides valuable Tier 1-3 information on CH damage/degradation, essential for risk and resilience models. D6.1 is an important document where procurement and processing of multiscale remote sensing data, as well as operational functions of the monitoring system are being reported.

All the information reported in the D6.1 deliverable document, will form a basis for HYPERION WP6 implementation. Links to HRAP in order to connect degradation and damage assessment with resilience procedures are also included.

1.2 Scope and Objective

The Remote Sensing-based multiscale monitoring system aims at providing detection of damage/degradation and emerging hazards for the individual CH monuments (tier 1) that are reported in D2.1, as well as for the broader area (tier 3) of the pilot areas (i.e. city of Rhodes, Granada, Venice and Tonsberg). Furthermore, it aims at rapid post-hazard event damage assessment of the CH assets and the broader area. RS-MMS integrates data from various remote sensing platforms such as satellites, UAV and ground based, with the focus on the optimal processing of remote sensing data in order to match the specific monitoring needs for historic monuments/areas and hazard scenarios. The Ground Control System (GCS) and Generic Ground Station (GGS) are the main components of the RS-MMS responsible for data acquisition and processing, respectively. The products of the GGS will be stored in the repository of the RS-MMS which will enable connection between the generated degradation/damage information with the hazard and resilience assessment procedures.

2. The components of the RS-based multiscale monitoring system

The RS-based multiscale monitoring system is presented in Figure 1. The Ground Control System is responsible for data acquisition by air and ground-based platforms. It includes tools for path planning, navigation and control of the vehicles, as well as photogrammetric devices and laser scanners. It aims at the acquisition of data for Tier 1 buildings. Furthermore, satellite remote sensing data will be selected enabling the activation of Tier 2 and Tier 3 monitoring levels. Remote sensing data and Copernicus products from the Emergency Management Service (EMS) will be collected, processed, analysed and integrated in the HYPERION Generic Ground Station (GGS). Advance methodologies for a) 3D analysis using photogrammetric means and ML, mainly focusing on deep learning methodologies and tensor Algebra decomposition b) ground deformation assessment using SBAS approach, c) change detection using deep learning methodologies, and d) flood extent delineation based on Bayesian approach will be employed for generating the RS-MMS products.

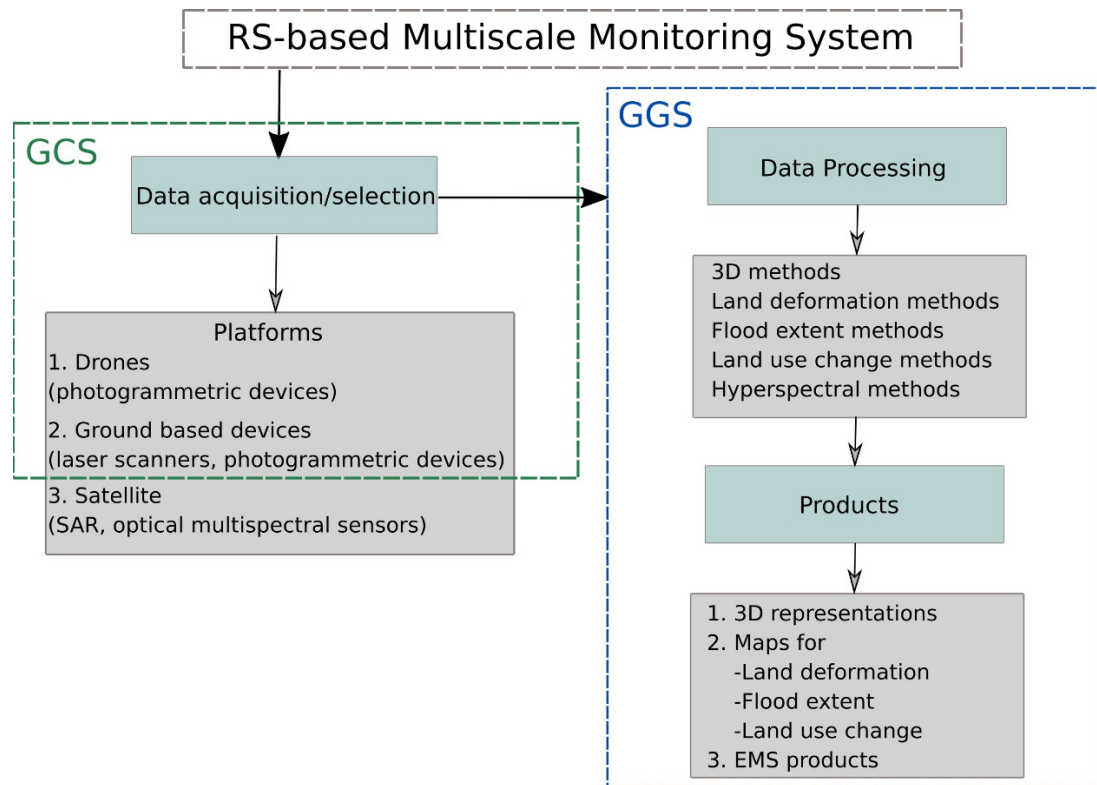


Figure 1: The RS-based multiscale monitoring system

2.1 The data acquisition/selection component

2.1.1 GCS deployment

The GCS contains all the necessary equipment for the data acquisition process and the in situ monitoring of the CH buildings. The system needs to be transportable in order to move it to all the Cultural Heritage Buildings and Sites that need to be monitored.

The system includes multi-rotor and/or fixed wing, depending on special local conditions, UAS combined with terrestrial or airborne multispectral, hyperspectral and thermal cameras, digital high resolution cameras, laser scanners and integrated total stations with all the necessary accessories. The equipment will be used for the 3D modelling, monitoring and representation of the selected structures and the immediate surroundings.

First of all, the UAS has three components:

- An autonomous or human-operated control system which is usually on the ground but may also be on another airborne platform
- An Unmanned Aerial Vehicle (UAV)
- A command and control (C2) system or sometimes referred to as a communication, command and control (C3) system which links the vehicle and the system.

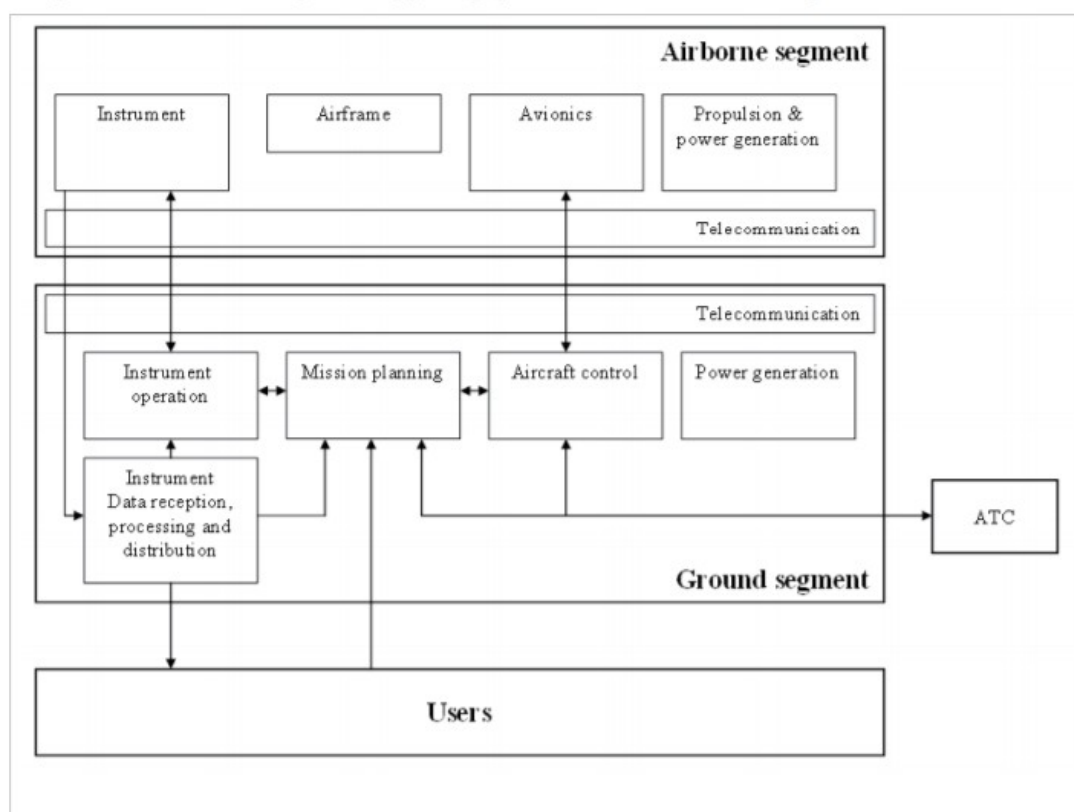


Figure 2: Overview of the UAS components. (Everaerts, 2008)

The airborne component consists of the airframe, the avionics with a central processing unit, the location transponder, the power and propulsion system, the instrument and the telecommunication (Everaerts, 2008). On the other hand, the ground component is composed of the mission planning, the aircraft control, the telecommunication, the instrument operation, the instrument data reception, processing and distribution. This whole system is responsible for the effectiveness and functionality of the airborne and the ground segment operation, the mission preparation, monitoring and inspection.

Moreover, close range photogrammetric methods will be conducted using high resolution digital cameras as well as terrestrial laser scanners. Although image-based modelling with digital high resolution images could be sufficient, experience

from previous implementations (Tapinaki et al., 2019; Moropoulou et al., 2017) has shown that for determining the surface of the object laser scanning delivers equally accurate but crisper point clouds compared to the SfM-MVS (Structure from Motion, SfM-MultiView Stereo, MVS) procedure.

The raw data for the 3D modelling of the CH buildings and sites will be measurements, images and point clouds. The size of the data will vary according to the size, level of detail and complexity of each CH site and it is estimated to be 25-40GB.

2.1.2 Satellite images

SAR data

SAR sensors have the advantage of providing information at all weather (cloud-free), illumination (day and night) conditions over a site. Modern SAR sensors such as Sentinel-1 can offer reliable, repeated wide area monitoring provide information at a systematic way. Due to the abovementioned advantages of SAR data, a lot of studies were conducted the past two decades for extracting land deformation information (Massonet et al., 1998, Yunjun et al., 2019) and for flood mapping and monitoring (Twele et al., 2016).

The [Sentinel-1](#) mission is the European Radar Observatory for the Copernicus joint initiative of the European Commission (EC) and the European Space Agency (ESA). The Sentinel-1 mission is a two-satellite constellation and includes high-resolution dual polarization C-band imaging at very short revisit times (6-days) and rapid product delivery. Sentinel-1A/B satellites were successfully launched in 2014 and 2016 respectively. Moreover, the free, full and open data policy adopted for the Copernicus programme foresees access available to all users. Sentinel-1 is designed to work in a pre-programmed mode imaging all global landmasses ensuring the reliability of service required by services and a consistent long term data archive built for applications based on long time series.

In Figure 3, the coverage of Sentinel-1 data over the pilot areas is denoted with red rectangles. Around 120 Sentinel acquisitions were selected for each pilot area for the period 2016-2019. The Sentinel-1 IW TOPS data were downloaded from <https://scihub.copernicus.eu/>. The total size of the SAR datasets is around 2.2 TB.



Figure 3: Sentinel-1 footprints (red rectangles) for pilot areas

High resolution optical multispectral data

Sentinel-2 is a wide-swath, high-resolution, multi-spectral imaging mission, supporting Copernicus Land Monitoring studies, including the monitoring of vegetation, soil and water cover, as well as observation of inland waterways and coastal areas. The Sentinel-2 Multispectral Instrument (MSI) samples 13 spectral bands in the visible, near infrared, and short wave infrared part of the spectrum: four bands at 10 meters, six bands at 20 meters and three bands at 60 meters spatial resolution.

The acquired data, mission coverage and high revisit frequency (5 days) of the twin satellite constellation provides for the generation of geoinformation at local, regional, national and international scales. Sentinel-2A/B satellites were successfully launched in 2015 and 2017 respectively. The Sentinel-2 mission is part of the Copernicus programme and like all Sentinel data follow the free, full and open data policy. The Sentinel-2 data can be downloaded from <https://scihub.copernicus.eu/>.

The Operational Land Imager (OLI) is one of the two instruments carried on board Landsat 8 (also known as LDCM - Landsat Data Continuity Mission) satellite. This sensor provides seasonal coverage of the global landmass at a spatial resolution of 30 metres (visible, NIR, SWIR) and 15 metres (panchromatic). The spectral coverage and radiometric performance (accuracy, dynamic range, and precision) are designed to detect and characterize multi-decadal land cover change in concert with historic Landsat data. The objective of scheduling and data collection is to provide cloud-free coverage of the global landmass on a seasonal basis. The main objective of ESA's implementation of the Landsat 8 PDGS is the provision of the LDCM data to the European user community within 3 hours after the sensing time. Landsat 8 was launched in 2013. The Landsat 8 OLI data can be downloaded from

<https://landsat8portal.eo.esa.int/portal/>. In Figure 4, the footprints of Sentinel-2 (red) and Landsat 8 (green) data over the areas of interest is presented.

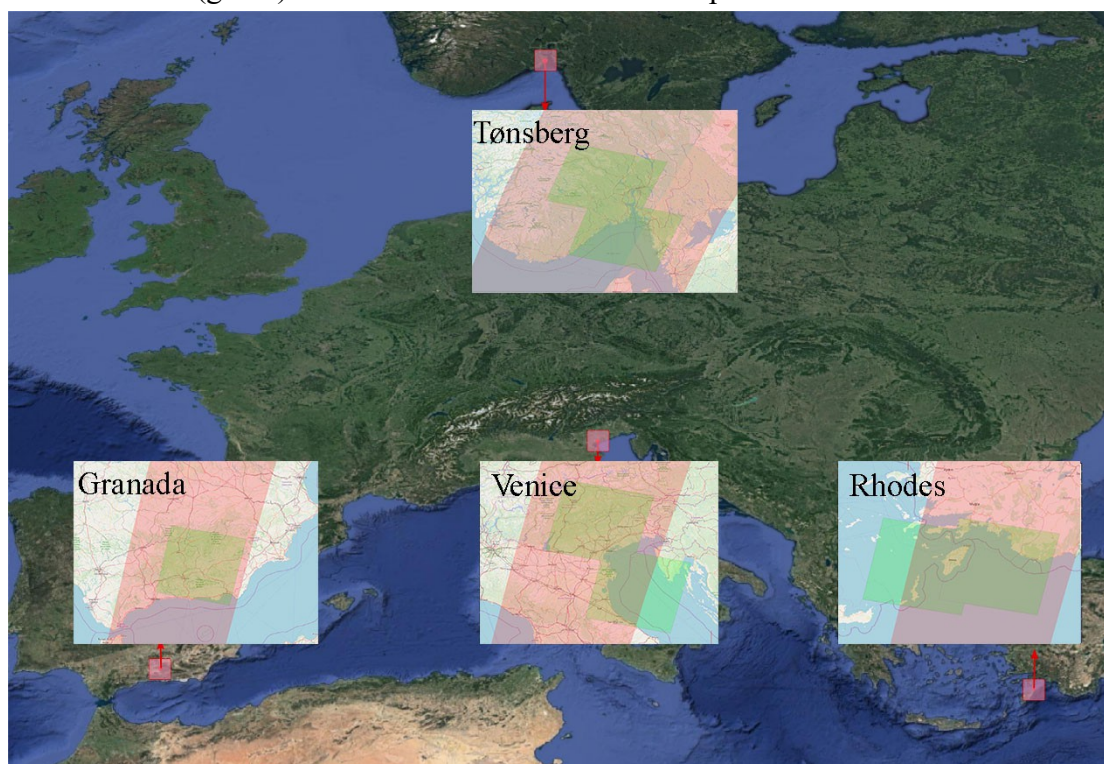


Figure 4 Sentinel-2 (red) and Landsat 8 (green) footprints for pilot areas

For the pilot areas of the Hyperion project, given the number of orbits of each satellite over each area, their revisit frequency varies between 1 to 5 days. The revisit frequencies and the number of orbits for each satellite and each pilot area are presented in the table below.

Table 1 Satellite revisit frequency

Pilot Area	No of S2 orbits	No of L08 orbits	Revisit frequency (days)
Rhodes city	1	2	(1 - 5)
Granada	1	1	(1 - 5)
Tonsberg	2	2	(1 - 3)
Venetia	1	2	(1 - 5)

Very high resolution optical multispectral data

Very high resolution (VHR) satellite images contain the necessary spatial resolution (<1 m) for the monitoring of the increase of impervious surfaces. Thus, the land cover changes of the four cultural heritage areas will be monitored by VHR satellite images collected by three commercial satellites owned by Digital Globe in the years 2010 and 2019. The selected images are provided a) by Quickbird with spatial resolution 0.61 m in the panchromatic (PAN) band and 2.4 m in the multispectral bands (MS), b) by WorldView-2 (WV-2) with spatial resolution 0.46 m in the PAN band and 1.84 m in the MS bands and c) by WorldView-3 (WV-3) with spatial

resolution 0.31 m in the PAN band and 1.24 m in the MS bands. Quickbird was operational until 2015 while WV-2 and WV-3 are still operating. The land cover change detection method will make use of the pansharpened visible and near infrared bands. The total size of the optical multispectral data provided by the abovementioned satellites is around 5 GB. If the size of the pansharpened and resampled data (required in pre-processing steps) is taken into account, the total size is around 20 GB.

2.2 The data processing component

2.2.1 The Ground Generic Station concept

Data from ground and drone sensors, as well as, satellite imagery and Copernicus products will be collected, processed, analysed and integrated in the HYPERION Generic Ground Station (GGS) to address multiscale monitoring requirements ranging from the historic areas and the ambient environment to detailed inspection of selected hotspots.

Practically, the GGS will be a server dedicated to perform all the data collection as well as to do most of the remote sensing data pre-processing, processing and storage of the results. To do this, the server, will have a fast network connection (in order to achieve fast transfer of the HYPERION raw airborne or satellite data), will hold a large storage volume and will have high computing efficiency. Inside the server, dockerized applications and/or virtual machines, each one dedicated to perform different tasks (more than one if compatible one another), will perform the data processing. Algorithms and methodologies for monitoring floods, ground deformations and land cover changes will be developed. Terrestrial and airborne data will be processed and novel methodologies will be applied for 3D models, 4D representations, and change detection approaches appropriate to detect structural deformations. The output of the processing methodologies will be hosted on the MMS product repository, which can also be hosted on the same server along with GGS. Thus, the GGS as delineated in Figure 1 and the MMS product repository, which is described in MMS product repository, will most probably be hosted on the same machine, which will also have the task to communicate with HRAP via the middleware.

2.2.2 3D representation methods

The aim of the raw data processing stage is to produce accurate 3D models of the monuments to be monitored, in order to have all the necessary geometric information of the case studies. The data processing procedure could be divided in two parts, one concerning the digital images and the other one concerning the laser scanner point clouds.

As far as the first process is concerned an image based modelling software will be used in order to produce the dense point cloud. This kind of software uses contemporary computer vision algorithms suitably adapted to confront the challenge of processing a huge number of images and extracting useful metric information from them. Structure-from-Motion (SfM) from unordered images has seen a tremendous evolution over the years. SfM is the process of reconstructing the 3D object structure from its projections into a series of images taken from different viewpoints (Schönberger & Frahm, 2016). It commonly starts with feature extraction and matching, followed by geometric verification. The result is a refined 3D reconstructed sparse point cloud using most of the times filtering processes and bundle adjustment.

Then, the output of SfM serves as the input to MVS to obtain a dense representation of the scene, e.g., in the form of depth maps, a dense point cloud, or a meshed surface model (Schönberger, 2018). Generally, the ultimate goal of image-based reconstruction is to produce high-quality 3D models. The quality of SfM results strongly depends on accurate and complete two-view correspondences as input, and MVS relies on an accurate and complete SfM reconstruction. As far as the laser scanning process is concerned, the common practice followed is the registration of the point clouds, either using the Cloud-to-Cloud method or using the Target-to-Target method. The registered point clouds will be further processed to reduce noise and remove unwanted objects. Then the dense point cloud from the IBM software will be used to fulfil the scans and generate the final point cloud for each CH building. Finally, the point object will be converted to a polygon object and any deviation will be fixed.

3D survey methodologies employing both TLS and close-range photogrammetry with SfM techniques will produce accurate and detailed 3D models. This will be an effective solution in order to monitor and identify any differential movements, deflections and cracks in the CH buildings.

2.2.3 Satellite image processing methods

In this section the processing workflows using satellite remote sensing data are described.

Methodology to extract ground displacement from SAR satellite data

SAR data contain backscattering intensity information and phase information of the ground. Backscattering reflects the surface properties (water content, roughness etc.) and phase records contains distance information between the sensor and the target. The technique that combines the SAR acquisitions to provide topographic or ground deformation estimation is called InSAR (Interferometric SAR). InSAR is the measurement of signal phase change (interference) between radar images (over time). Considering a single pixel footprint on the ground P , the sensor acquires a first SAR image from satellite position M , measuring a phase ϕ_1 and from a second satellite position S measuring a phase ϕ_2 . The Interferometric SAR (InSAR) technique exploits the phase difference :

When a point on the ground moves, the distance between the sensor and the point changes, thereby producing a corresponding shift in signal phase. This shift is used to quantify the ground movement.

Where $\Delta\phi$ is a phase shift due to different atmospheric conditions between the two acquisitions

An interferogram is a 2D representation of the difference in phase values. Variations of phase in an interferogram are identified by fringes, colored bands that indicate areas where movement is occurring and the rate of movement being experienced. The precision with which the movement can be measured is usually in the centimeter range as the phase shift is also impacted by topographic distortions, atmospheric effects, and other sources of noise.

When InSAR is used to identify and quantify ground movement the process is referred to as Differential InSAR (DInSAR). In DInSAR topographic effects are removed by using a DEM of the area of interest to create a differential interferogram.

is the contribution to phase arising from possible errors in the DEM that was used to remove the topographic effects, is the differential interferometric phase, is the incremental distance the signal travels from the sensor to the ground and back, and is the atmospheric contribution to phase shift.

DInSAR is a useful tool for identifying footprints of progressing movement and creating deformation maps. The limitation of DInSAR method results from DEM errors, atmospheric propagation delays and decorrelation due to the increase of the temporal and spatial baseline between satellite passes. Moreover, DInSAR technique has relatively low precision (centimeter scale) and it cannot distinguish between linear and non-linear motion. To overcome these difficulties and produce long time series of ground motion, two groups of interferometric time series methodologies have been developed. The first one is called Permanent Scatterer (PS) (Ferretti et al., 2001; Hooper et al., 2004) and extracted displacement information over high-coherent targets. The second one is called Small Baseline Subset (SBAS) (Berardino et al., 2002; López-Quiroz et al., 2009; Yunjun et al., 2019) and can extract deformation information also over medium-coherent targets. The efficiency of both approaches has been proven in numerous applications (Yan et al., 2012).

Due to the improved orbital control and short revisit time of Sentinel-1, the SBAS method has a great potential for extracting ground deformation from a time series of differential interferograms (Yunjun et al., 2019). The main principle of SBAS technique is to exploit redundant information from a network of interferograms with small temporal and spatial baselines. The redundancy is resolved using (weighted) least square estimation (Lauknes et al., 2011; Yunjun et al., 2019) for fully connected interferograms networks or singular value decomposition (Berardino et al., 2002; López-Quiroz et al., 2009) in case of non-fully connected networks. The work of Yunjun et al., 2019 and the developed software [package](#) will be used as basis for the GGS land deformation component. A short description is provided at the next paragraphs.

Let's say that a system of interferograms from SAR acquisitions that have to be inverted to extract the deformation information, is expressed by the following relationship:

Where

is the differential interferometric phase of the interferogram,

is a $N \times (N-1)$ design matrix indicating the acquisition pairs used for

interferograms generation. It consists of -1, 0 and 1 for each row with -1 for master acquisition, 1 for slave acquisition and 0 for the rest.

is the error term of the interferograms. This error term includes the decorrelation noise, the phase change due to change of dielectric properties of the target (De Zan et al., 2014) or processing inconsistencies such as co-registration, interpolation errors (Agram and Simons, 2015) and unwrapping errors.

For fully connected interferograms networks the full rank design matrix A can be inverted using an unbiased weighted least square estimator on the overdetermined system (Yunjun et al., 2019).

where is the estimated raw deformation phase time-series and

is a $n \times n$ diagonal weight matrix,

According to (Tough et al., 1995), the inverse of phase variance can be a representative metric that can be used as weighting factor. The phase variance is calculated through the integration of phase probability distribution function (PDF).

At a second and final stage, the de-noising of the estimated raw deformation phase time-series from topographic residual, tropospheric and phase ramp components is performed. For this project, a special treatment of these contributions will be performed due to the available data from end-users of each pilot case. In particular, exploiting the already provided recently-updated high resolution DEM/DSM information the topographic residual term can be mitigated with an approach based on Fattahi and Amelung, 2013. Tropospheric contributions will be estimated and subtracted using data from meteorological stations based on the approach from Dong et al., 2019. GPS data will be used for estimating linear or quadratic ramps introduced by orbital errors based on the work of Tong et al., 2013. Finally, a part of GPS measurements will be used as validation for the deformation results over the pilot areas.

Methodology for landslide mapping and earthquake induced deformation

Fast response after natural disasters, such as earthquakes and landslide, is necessary to support actions related with rescue, humanitarian and reconstruction operation in the affected area. Rapid damage mapping after a disaster is crucial and can provide a first damage assessment for the affected region. Satellite remote sensing data due to their low cost, wide coverage and frequent observations play a key role to this manner. Algorithms that based on the processing of SAR data due to their all day all weather availability are considered excellent choices (Plank, 2014).

Well-established procedures for damage assessment using SAR data are based on coherence and intensity correlation approaches. For example, Yonezawa et al. 1999, investigated damage assessment of urban area after the 1995 Hygokon-Nanbu Earthquake, Japan and the 2001 Gujrat Earthquake, India using a normalized difference approach in interferometric coherence. Fielding et al., 2005 performed damage assessment by visual interpretation of the interferometric coherence after the 2003 Bam Earthquake. Chini et al., 2008 used ERS and ENVISAT ASAR data and determined surface changes caused by the 2004 Indonesia Earthquake by visual interpretation of SAR intensity coefficient and SAR backscattering. The reported a higher accuracy of their damage assessment when SAR backscattering and intensity correlation are combined into RGB combinations compared to single use of SAR backscattering or intensity correlation. Mondini et al., 2019, applied photo-interpretative methods to detect landslide in measures of change of amplitude in pre- and post-event Sentinel-1 images.

For the HYPERION project for each pilot area, an automatic processing chain that will generate, an information stack of a) pre-, post-disaster calibrated backscattering, b) intensity correlation, c) interferometric coherence, and d) wrapped interferogram, will be developed as a part of GGS.

Methodology to derive floods

Flash floods are considered to be among the most frequent and destructive types of natural disasters worldwide, with significant consequences including: (a) human and animal life losses, (b) agricultural crops destruction and soil loss (c) damages of infrastructures, communication networks, and, (d) transport of sediment loads and pollutants. The most efficient way of mapping flood extents in near real time and over large areas is to exploit EO satellite images. The best practise is to use synthetic aperture radar (SAR) images due to their almost all-weather day/night image acquisition capabilities (Giustarini et al., 2016). Flat surfaces such as calm water appear as dark areas in a radar image (decreased backscattering coefficient, σ_0), since most of the incident radar pulses are specularly reflected away from the antenna. Although, in built environments, vegetated canopies, deep valley bottoms, and various surface waterlike response areas, σ_0 increases if the radar wave bounces of the water and then off a vertical structure (the “double bounce” effect). Moreover, as a consequence of the side-looking nature of SAR sensors, areas of a ground surface may not be visible to the satellite due to radar shadowing and layover caused by buildings or taller vegetation (Lin et al., 2019).

Commonly used SAR-based flood extent mapping techniques include simple visual interpretation, supervised classification, histogram thresholding, interferometric SAR coherence, and various multitemporal change detection methods. Histogram thresholding is one of the most commonly used methods. Giustarini et al., 2016, given a SAR image of backscatter values, constructed a total histogram of backscatter values and decompose this histogram into probability distribution functions of backscatter values associated with flooded (open water) and non-flooded pixels, respectively. Several studies have tried to improve the accuracy of urban flood mapping by addressing layover and shadow effects, such as Mason et al., 2012, by masking out the layover and shadow zones by using a SAR simulator. Pulvirenti et al., 2011, developed an algorithm that adopted the double-bounce intensity values from electromagnetic modeling as initial fuzzy thresholds, and they used fuzzy logic to map out the urban flood with intensity increase.

Moreover, multitemporal SAR data analyses are also being adopted by scientists to study flood extents. Hostache et al., 2012 suggested to select the most appropriate pre-flood image for change detection from a time series perspective. Schlaffer et al., 2017, carried out harmonic analysis on seven years of ENVISAT ASAR data and identified floods by looking at anomalies in the time series. Based on the Giustarini et al., 2016, study, Lin et al., 2019, applied a time-series normalization on the backscattering data and then used the probability distribution functions for intensity decrease (due to specular reflection of the signal) and intensity increase (due to double bounce) cases separately.

In addition, some studies have found that using interferometric coherence in conjunction with intensity will improve the detection accuracy particularly associated with double bounce. Pulvirenti et al., 2016, showed that a significant improvement in the detection of urban flooding could be made by using SAR coherence in conjunction with backscatter to detect the flooding. Coherence was measured using the phases and amplitudes of interferometric pairs, with one image being obtained

during the flooding, and the other prior to the flooding. An urban area that is not flooded should have high coherence whereas if there is flooding the coherence should be low. Chini et al., 2019, introduced an approach that is based on two fundamental processing steps: the first one exploits a multi-pass technique to detect areas of double-bounce in an urban environment; the second one uses the change of within those areas to detect the inundated pixels.

Complementary to SAR images, optical data also have been used to monitor flood events. D'Addabbo et al., 2016, presented a data fusion approach, based on Bayesian Networks, where multi-temporal SAR intensity images, multitemporal InSAR coherence data and optical data are fused together. For wetland and flood monitoring, Toyra et al., 2005, used the augmented vector approach to combine radar data and optical images from Landsat or SPOT as if they were obtained by one sensor. To extract flooded area and water body, Sun et al., 2007 considered the principal components analysis and the intensity, hue and saturation method to combine infrared Landsat bands and radar data. Dey et al., 2008, considered a decision fusion approach to combine classification results from Radarsat and Landsat data to distinguish between permanent water and flood regions. Li and Chen, 2005, applied a decision rule technique using Radarsat 1, Landsat 7 and DEM data for wetlands mapping. Optical satellite data may be helpful in urban flood mapping due to the higher spatial resolution than SAR data but oftentimes cannot be exploited due to cloud coverage or potential false alarm because of shadows.

An approach enabling the automated, objective, and reliable flood extent extraction from Sentinel-1 SAR, and Sentinel-2 and Landsat 8 optical imagery (if they pass the cloud constraint) will be developed. Estimation of the probability density function of backscattering values associated with “open water”, appropriate thresholding, which yields a flood inundation map, and detection of permanent water bodies will be key factors for the effectiveness of the developed approach.

Methodology for detection of land cover changes

Deep learning is among the machine learning techniques that have proven very promising results in multiple image processing tasks in the current research. The increasing computation capabilities provided by modern central processing units (CPUs) and especially graphical processing units (GPUS) combined with the existence of public databases with large training data, have permitted the development of robust artificial neural network architectures.

Artificial neural networks simulate the processes of the human brain and are capable of representing both low level and high level features. Among their well-known advantages are the absence of the need to create time-consuming human-engineered features and their ability to be less sensitive to noisy training data compared to other machine learning methods. Convolutional neural networks use convolution as a key concept in order to represent spatial information besides the spectral. CNNs can either appear as patch-based architectures or more recently as pixel based encoding/decoding architectures which are fully convolutional, i.e. they do not contain fully connected layers. The depth of the network, the activation functions, the kernel size, the number of feature maps, pooling/deconvolution layers for downsampling/ upsampling etc. consist critical hyperparameters when building a CNN architecture.

Since image classification is among the most fundamental image processing tasks, the majority of the deep learning architectures were initially developed to target the classification problem. Change detection can be thought as a form of image classification which uses multitemporal imagery as its input.

For the HYPERION project the following methodology will be followed for the land cover change detection. At first, resampling of the multitemporal images will be implemented in order to achieve common spatial resolution between the images collected by the different satellites. Then, image registration will be performed (Figure 5) which is the process of geometrically aligning images covering the same scene obtained at different times (Zitova & Flusser, 2003). Three main steps are included in image registration: collecting matched point-pairs, establishing a transformation model, and transforming images. The matched point-pairs are either manually or preferably automatically selected. Well-known methods that automatically detect salient and distinctive features include SIFT (Lowe, 2004) and SURF (Bay et al, 2008). Difficulties in image registration are imposed by the radiometric difference between multi-temporal images caused by different imaging conditions and different spectral sensitivity of the sensors. Calculation of robust texture features (Gabor features) (Cerra et al, 2016) will be considered to mitigate possible radiometric differences that affect the land change detection method.

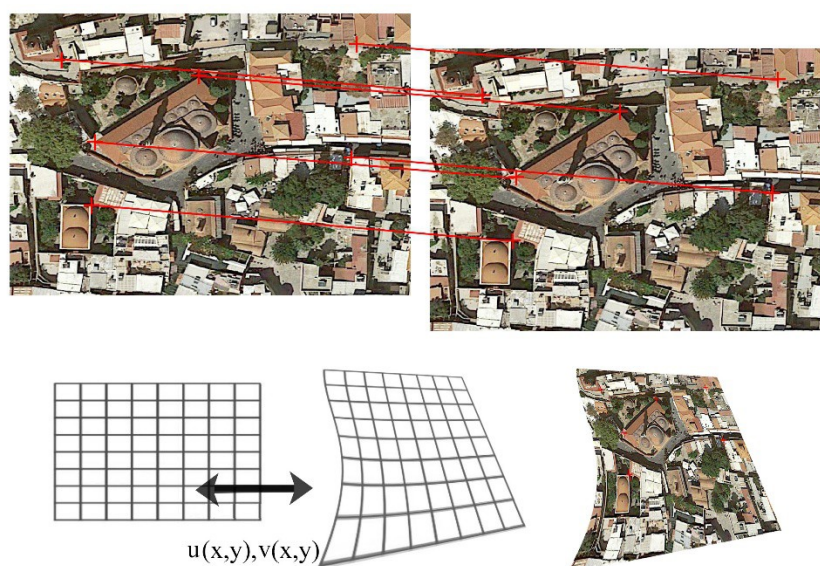


Figure 5: Image registration process

Following image registration, the land cover change detection method will be developed. The semantic richness of VHR images increases the complexity of the image analysis and makes the change detection process even more challenging especially in complex and heterogeneous environments like those studied in the project. Thus, the methodology will be based on most recent deep learning approaches in order to mitigate these challenges. The method will observe changes for the years 2010 and 2019 in the four cultural heritages areas studied in the project (Figure 6). This time frame was considered suitable since it is expected to provide an adequate

number of land cover change training data necessary for the development and implementation of the methodology.



Figure 6: Heterogeneity of land cover in the areas studied in the project. a) Granada, b) Tonsberg, c) Rhodes, d) Venice

The methodology will investigate a) Early Fusion (EF) which consists of concatenating the two multitemporal image pairs as the first step of the network and b) Siamese networks (Figure 7) where each of the patches are processed in parallel by two branches of convolutional layers usually with shared weights. Both a supervised end-to-end approach (Daudt et al., 2018; El Amin et al., 2016; Lin et al., 2019;) as well as an unsupervised approach (De Jong & Bosman, 2019; Wu et al., 2019) will be investigated in order to successfully monitor the increase of impervious materials. Training data will be manually extracted by the multitemporal images provided by Quickbird and WV-2, WV-3 VHR satellites. Possibly available land cover maps (e.g. European Settlement map) will assist in the labelling process. Simple processing techniques such as band subtraction / ratio and spectral vector angle will also give a preliminary indication of the changes.

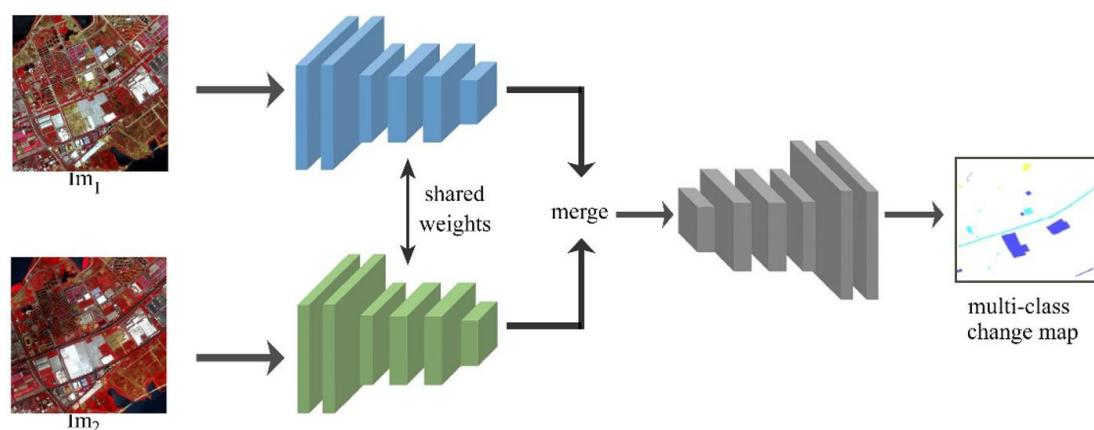


Figure 7: Indicative example of a Siamese convolutional neural network with decoder structure. Source of input images: Wu et al., 2019

2.2.4 Hyperspectral methods

The recent advances in optics and photonics have stimulated the deployment of hyperspectral imaging sensors of high-spatial and high-spectral resolution. These

sensors are now placed on satellite, unmanned aerial vehicle, and ground acquisition platforms used for material, object, and terrain land detection and classification (Wycoff, 2013). In this context, hyperspectral information can be valuable for damage detection and monitoring of structural health of cultural heritage sites.

In hyperspectral image analysis, although high-spatial and high-spectral resolution improves classification accuracy, it also imposes several research challenges derived as a consequence of the so-called “curse of dimensionality”; the difficulties arise when we need to analyze and organize data in high-dimensional spaces. Hyperspectral data have their own unique characteristics, though being applied for a wide variety of applications, such as agriculture, surveillance, astronomy, and biomedical imaging (Chang, 2013): 1) high-dimensional data; 2) limited number of labelled samples; and 3) large spatial variability of spectral signatures (Camps-Valls, 2004).

Several works in the literature concerning hyperspectral image classification, follow the conventional workflow of pattern recognition process, consisting of two separate steps. First, features are extracted from the raw data, creating labelled training data sets. Second, classifiers, linear or nonlinear, such as support vector machines (SVMs) and neural networks (NNs), are used to map the extracted features to the target (desired) outputs. The key problem, however, in applying such conventional processes in classifying high-dimensional hyperspectral data is that a large number of labelled training samples are required to model the statistical input diversities and consequently to well train the classifier. In remote sensing applications, a collection of a large number of labelled data is an expensive and time-consuming process. Another drawback is that classifiers are often used as “black boxes”. This means that there is no direct interpretation of how spatial and spectral bands contribute to the final classification outcome.

One way to address issues deriving from the high dimensionality and heterogeneity of the data is to employ statistical learning methods [6]. However, even in this case, the problem of extracting a set of appropriate features remains. Feature representation significantly affects the classification outcome. Estimating a suitable set of discriminative features, in order to increase the accuracy of the classifier, is an arduous task especially when the data is lying in high-dimensional spaces.

For this reason, recently deep learning paradigms have been investigated for classifying hyperspectral data (Hinton, 2006). Deep learning machines receive as inputs, instead of features, the raw sensory data. Then, they nonlinearly transform the raw inputs to hierarchies of representations which are used, in the following, as “the most suitable features” in a supervised mapping phase. Thus, deep learning tackles feature-related issues. This is also proven by the current research outcomes (Chen, 2014; Makantasis, 2015a) indicating the outperformance of deep learning machines in accurately detecting various objects in hyperspectral imaging data. Examples include the detection of man-made constructions rather than natural ones (Makantasis 2015b), vehicles’ detection, object tracking (Kandylakis, 2016), land cover mapping, and critical infrastructure assessment (Makantasis, 2016). In the context of HYPERION, we will implement deep learning models, such as Convolutional Neural Networks and variations thereof for hyperspectral image classification.

However, typical deep learning approaches are not without shortcomings. A typical deep learning architecture contains a huge number of tuneable parameters implying that a large number of samples is also needed to accurately train the network. In addition, deep learning processes present high computational complexity.

Recently tensor-based machine learning models have appeared as promising alternatives for hyperspectral data classification (Zhou, 2013; Tan, 2012). In particular, Zhou et al. (2013) and Tan et al. (2012) have introduced a linear model using tensor-based regression with applications in neuroimaging data analysis and for classification. These approaches are considered as the first works which discussed the statistical inference procedure for the general raw tensor regression. In conventional learning models, usually the inputs are vector data. Therefore, in the case of multidimensional input arrays, first tensor vectorization is carried out. However, vectorization destroys the inherent spatial and spectral structure of the input which can offer a physical interpretation of how spatial information and spectral bands contribute to the classification outcome. Furthermore, tensor vectorization fails to address the issues that stem from the high dimensionality of the data, since again a large number of tuneable parameters are required. To handle these limitations, we need to consider the input data as tensors, keeping the spatial and spectral structure of the data, and then, using principles of tensor algebra, to find out ways to reduce the number of parameters needed to be estimated during training.

In HYPERION, we will develop tensor-based machine learning models in which through the decomposition of the model weights, we are able to significantly reduce the number of parameters required to train the classifier. Thus, a smaller labelled data set is needed than in conventional learning approaches where the tensor inputs are first vectorized. In this way, it will be made possible to adequately train learning models with fewer training data samples, which is one of the problems encountered in the case of hyperspectral imagery in HYPERION cultural sites in both routine monitoring and especially post-disaster damage assessment scenarios.

The tensor-based model to be employed is characterized by the rank-1 canonical decomposition property for the model weights, which means that it retains the structure of the spatial and spectral band information, which is a very important aspect for hyperspectral data classification. This is due to the fact that it actually permits the extraction of valuable information regarding the contribution of each of the hyperspectral bands to the classification. Thus, the canonical decomposition provides a physical interpretation of the classification outcome, i.e., how the location of the pixels (spatial information) and the spectral bands (spectral information) influence the final classification performance. The high-order nonlinear model relies on a modification of a feedforward NN (FNN), while it retains the universal approximation principles; capability of the network to approximate any unknown function, under some assumptions of continuity, within any degree of accuracy. The main difference is that the model weights satisfy the rank-1 canonical decomposition property. Therefore, the number of parameters (and consequently the number of training samples) is significantly reduced, especially for the cases where tensor inputs are considered.

3. MMS products

3.1 3D representations

The deliverables from the geometric documentation will be the three-dimensional models of the selected CH buildings and archaeological sites with no texture, just single coloured for presentation purposes. It is possible, if required, to deliver a shaded or textured 3D model for a selected case study. Furthermore, all the acquired high resolution images, as well as the point clouds will be available.



Textured 3D model of a bastion

The 3D model of the bastion without texture

Figure 8:3D representation products

The estimated size of the 3D model for each CH building and site will be 4-8GB. If needed, it is possible to reduce the file size, keeping at the same time a high level of detail.

3.2 Satellite remote sensing-based maps

3.2.1 Ground displacement results

The ground displacement estimation from the processing of SAR satellite data (Session 2.2.3) will result two kinds of products. The first product will be a vector map (collection of points) with deformation estimations at each SAR acquisition date. It is expected, that the points with deformation estimations are a subset of the initial points/pixels in the SAR acquisitions. The second product will be the deformation rate (velocity) for each point in a vector format and will be provided in a similar way as it is illustrated in Figure 9. The estimated volume of the products is approximately 2Gb per pilot area.

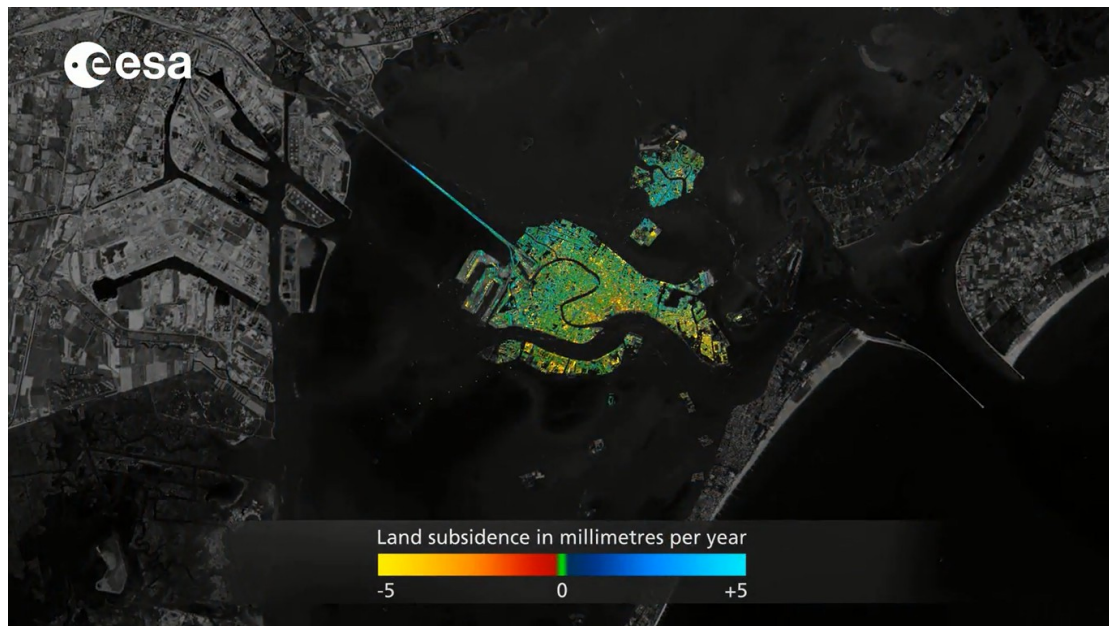


Figure 9: Ground deformation velocity map over Venice pilot area. Image Source: <https://sentinel.esa.int/web/sentinel/user-guides/sentinel-1-sar/applications/land-monitoring>

3.2.2 Earthquake and landslide results

After an earthquake or landslide event the information stack listed in 2.2.3 will be generated. An example of pre-, post-disaster calibrated backscattering and intensity correlation, is presented in Figure 10, for earthquake event. An example of pre-, post-disaster calibrated backscattering intensity is presented in Figure 11 for a landslide event. The information stack will be provided in raster format. The estimated volume is about of 300Mb per event.

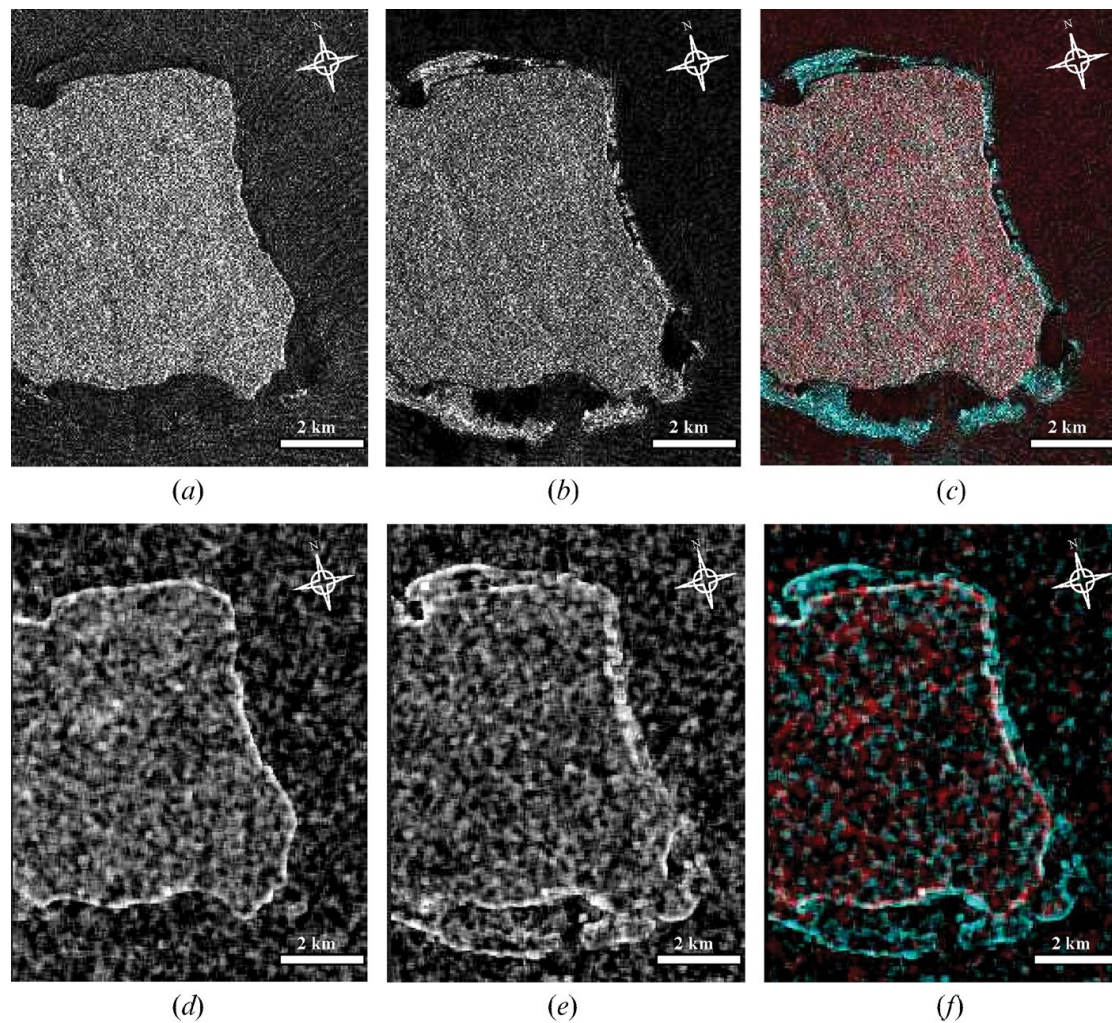


Figure 10: North Sentinel Island: (a) pre-seismic intensity image (b) post-seismic intensity image (c) RGB colour composite of intensity images ($R = \text{pre-seismic}$, $G = B = \text{post-seismic}$), where cyan regions represent emerged areas; (d) pre-seismic intensity correlation (e) post-seismic intensity correlation (f) RGB colour composite of correlation coefficients ($R = \text{pre-seismic intensity correlation}$, $G = B = \text{post-seismic intensity correlation}$), where cyan regions represent emerged areas. Figure taken from Chini et al., 2008

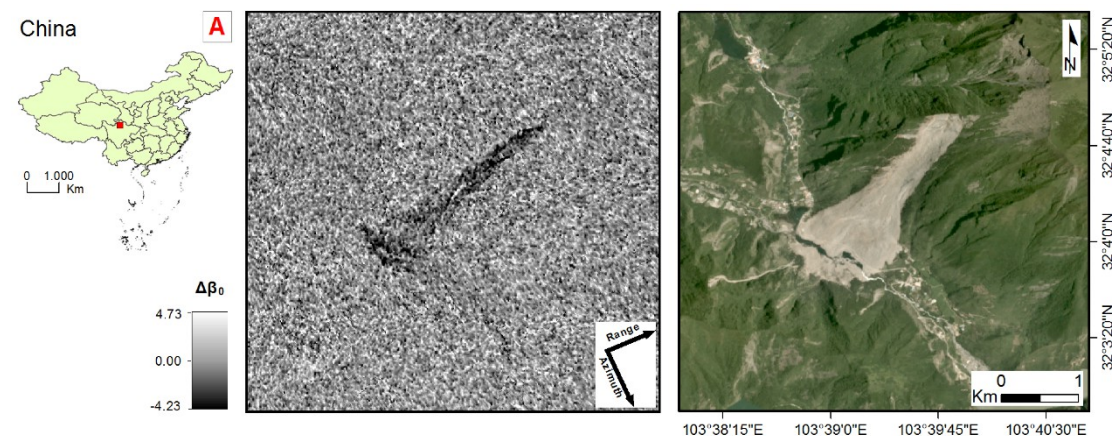
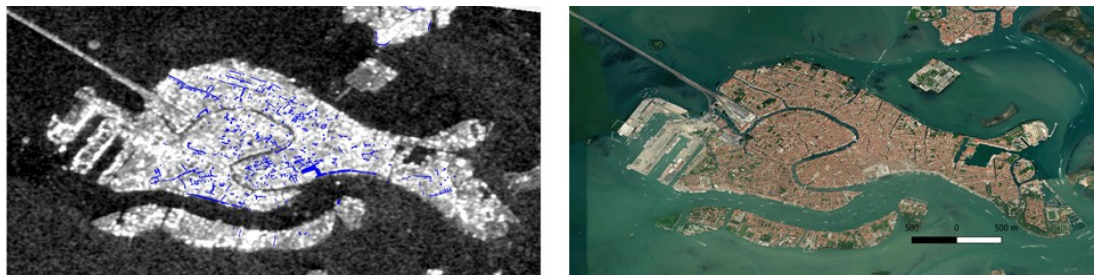


Figure 11: The Maoxian (China) landslide: On the left: landslide location, in the middle: the measure of SAR amplitude changes, on the right: the landslide in the optical image (from <https://www.planet.com>) Figure taken from Mondini et al., 2019

3.2.3 Flood mapping results

After a flooding event the process described in section 2.2.3 will be implemented in order to map the affected areas. The resulting product will be provided in vector format. An example a calibrated backscattering of a flooded area, is presented in Figure 12. The estimated volume is about of 300Mb per event.



3.2.4 Land cover change detection results

The land cover change detection results will be provided as a vector polygon map overlaid on the natural colour composite image of each cultural heritage area. Figure 13c shows an indicative example of a binary (changes/no changes) change detection map overlaid on an RGB natural composite (13d) and figure 14c shows a multi-class (categorical) change detection map. The categories will indicate if the change is related to vegetation, soil, or impervious material. The estimated size of the products for all areas is 2 GB.

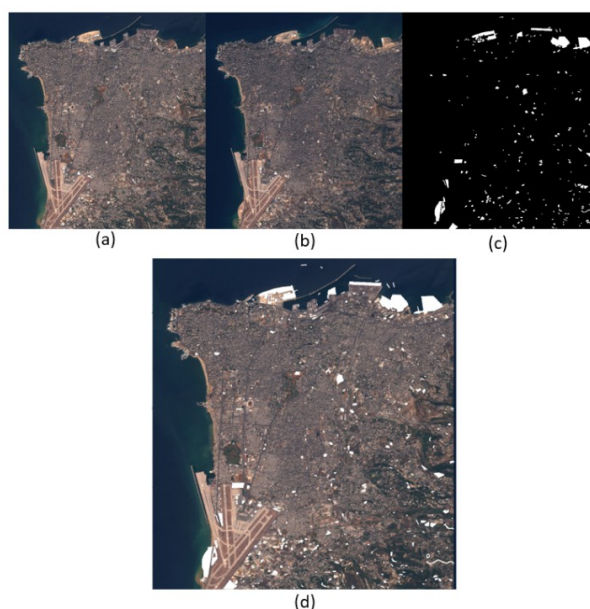


Figure 12:(a) RGB natural composite at time 1, (b) RGB natural composite at time 2, (c) change detection map, (d) change detection map overlaid on a natural composite. Source of figure: Daudt et al., 2018

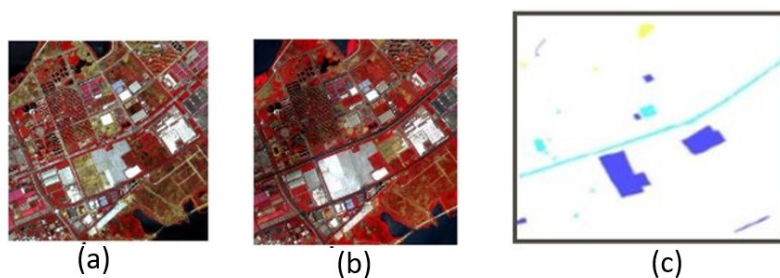


Figure 13:(a) pseudocolor RGB composite at time 1, (b) pseudocolor composite at time 2, (c) multi-class (categorical) change detection map. Source of figure: Wu et al.,2019

3.3 Copernicus EMS products

The Copernicus EMS Mapping addresses, with a worldwide coverage, a wide range of emergency situations resulting from natural or man-made disasters. Satellite imagery and other geospatial data are used to provide free of charge mapping service in case of a disaster throughout the world. The main disasters that are covered are: Floods, Earthquakes, Landslides, Severe Storms, Fires, Technological disasters, Volcanic eruptions, Humanitarian crises, Tsunamis. Copernicus EMS mapping consists of Rapid mapping and risk & recovery mapping services.

Rapid Mapping consists of the provision of geospatial information within hours or days from the activation in support of emergency management activities immediately following a disaster. Risk and recovery mapping consists of on-demand provision of geospatial information in support of Disaster Management activities not related to immediate response. This applies in particular to activities dealing with prevention, preparedness, disaster risk reduction and recovery phases.

EMS products will provide useful information for the history of natural or man-made disasters on the vicinity of pilot areas. Moreover, EMS products will be used together with HYPERION products to enhance the assessment of damage after disasters. An accuracy assessment of remote sensing based HYPERION products is also foreseen using EMS products as reference.



Figure 14:Flood Delineation product in Venice at 14/11/2019 10:13 UTC. Map source: <https://emergency.copernicus.eu/mapping/list-of-components/EMSR409>

4. MMS operational functions

4.1 Routine monitoring

Among the objectives of the RS-MMS is to provide suitable information for the routine monitoring of CH assets. Remote Sensing products enable the inspection of CH assets for hazards with slow or gradual onset. More analytically the routine monitoring will include:

Three-dimensional models of the selected CH buildings.

Displacement maps (velocity and deformation time series product) [see session 3.2.1]. The initial products will show displacements from the start of 2017 till the end of 2019. Then the maps will be updated every year.

Land cover change detection maps will be produced for each pilot area. Maps will highlight changes in the broader area for the period 2010 – 2019. Routine monitoring foresees the update of the maps every three years after the project lifetime.

Hyperspectral image maps depicting building materials will be produced during the lifetime of the project, indicating the construction material types, health and strength in every case. Such maps will also be produced in a routine monitoring context every three years after the project lifetime.

4.2 Post-disaster monitoring

After landslide, earthquake or flood event an alert will be triggered in the GGS and the respective remote sensing-based products [see Sessions 3.1.3, 3.2.1, 3.2.2, and 3.2.3] will be generated. Copernicus EMS products, if any, will also be downloaded in GGS. Similarly, hyperspectral imagery analysis will be performed to detect changes in the construction materials' health and strength and contribute to damage localization and assessment.

5. Communication with HRAP

5.1 MMS product formats

The output formats for the 3D models will be those of .ply, .obj, .wrl and/or .dxf. Moreover, any accompanying image files will have the .jpg, .png and/or .tiff format. If any image file need to be georeferenced, an extra file will be provided with the .tfw format.

Similarly, the output format of the satellite remote sensing-based products will mostly consist of raster (.tiff, .jpg, .png) or vector format maps (shapefile, GeoJSON, geodatabase).

High volumes of raw and processed information are expected to be stored in the MMS repository and therefore will be difficult to manage and recalled effectively unless proper metadata is also stored along with the data and the output products. This metadata has to incorporate in their structure all the information that identifies the different structures/phenomena highlighted in the associated images/products. For the exploration and discovery of the information hidden inside of the large MMS repository, new tools and methods have to be provided.

5.1.1 Metadata

Metadata is machine understandable information that describes a set of data. Metadata summarizes basic information about data, which can make finding and working with particular instances of data easier. The metadata to be shared and understood must respect the rules that guide the shape and structure.

The metadata have value if they are self-consistent and interpretable by systems and people. To do this we need to consider the directive that enabling the sharing of environmental spatial information: INSPIRE (Infrastructure for Spatial Information in the European Community). INSPIRE is an initiative to establish an infrastructure for in Europe that is geared to help to make or geographical information more accessible and interoperable for a wide range of purposes supporting.

We suggest XML format metadata file that not only complies with the INSPIRE directive but also ensures a greater degree of consistency and harmonization across data. Some standards that comply with this directive: INSPIRE profile of ISO 19115 ISO 19139 and ISO 19119.

Users will then have this ISO standards compliant metadata covering dataset language, reference, description, geographic location, temporal extent and date of revision, responsible party contact information, resource location and quality information including product lineage.

The general structure of the metadata is organized into different air macro, and each section must contain specific information. INSPIRE-compliant metadata are listed in the below list:

- Metadata
 - Point of Contact
 - Date
 - Language
- Identification
 - Resource title
 - Identifier
 - Resource abstract
 - Resource locator
 - Resource language
- Classification
 - Topic category
- Keyword
 - Keyword value
 - Keyword from INSPIRE data themes
 - Keyword from repositories
 - Free keyword
- Geographic
 - Geographic bounding box
 - Countries
- Temporal
 - Temporal extent
 - Data of creation
 - Date of publication
 - Data of last revision
- Quality & Validity
 - Lineage
 - Spatial resolution

- Conformity
 - Conformity
- Constraints
 - Conditions applying to access and use
 - Limitation and public access
- Responsible party
 - Responsible party

There are 3 type of metadata in general, and the attribute is different for each type:

- Series
- Service
- Dataset

In 2 the attributes for the three types of metadata are listed.

Table 2: the metadata attribute for the different type of metadata (series, dataset and service)

Metadata attribute	Mandatory / Obligation / Conditional	Series & Dataset	Service
Dataset title	M	X	X
Dataset reference date	O	X	X
Dataset responsible party	O	X	X
Geographic location of the dataset	C	X	X
Dataset language	M	X	
Dataset character set	C	X	
Dataset topic category	M	X	
Spatial resolution of the Dataset	O	X	
Abstract describing the dataset	M	X	X
Distribution format	O	X	X
Additional extent information for the dataset (vertical and temporal)	O	X	X
Spatial representation Type	O	X	X
Reference system	O	X	X
Lineage	O	X	X
On-line resource	O	X	X
Metadata file identifier	O	X	X
Metadata standard name	O	X	X
Metadata standard version	O	X	X
Metadata language	C	X	X
Metadata character set	O	X	X
Metadata point of contact	M	X	X
Metadata date stamp	M	X	X

5.1.2 Use of Metadata in the context of the HYPERION project

The need for the project is to prepare metadata to accommodate the specific characteristics of any particular CH hazard/phenomenon monitored, in adding to standard metadata. 3 presents the suggested standard structure for all image/map metadata, while custom metadata will have to be adjusted appropriately and added to it depending on the contents of each data layer in the MMS repository.

Table 3: Proposed standard attributes of raw image data and image/map products

Attribute	Father	Type
<i>Title</i>		String
<i>Source</i>		String
<i>Identifier</i>		String
<i>Abstract</i>		String
<i>Resolution</i>		String
<i>Temporal</i>	date/time	String
<i>Latitude</i>	geographic coordinate or point coordinate	Float
<i>Longitude</i>	geographic coordinate or point coordinate	Float
<i>North latitude</i>	geographic coordinate (box coordinate)	Float
<i>East longitude</i>	geographic coordinate (box coordinate)	Float
<i>South latitude</i>	geographic coordinate (box coordinate)	Float
<i>West longitude</i>	geographic coordinate (box coordinate)	Float
<i>Gemet_id</i> *	image_content_region - region_type	Integer
<i>Gemet_name</i> *	image_content_region - region_type	String
<i>AnyURL</i>	image_content_region - region_type	URL
<i>Dataset responsible party</i>		String
<i>Distribution format</i>		String
<i>Spatial representation type</i>		String
<i>Lineage</i>		String
<i>On-line resource</i>		String
<i>Season</i>	date/time	String
<i>Region name</i>	image_content_region	String
<i>Region geonames id</i>	image_content_region	Integer
<i>Geonames name</i>	image_content_region - administrative region	String
<i>Geonames id</i>	image_content_region - administrative region	Integer

* GEMET (General Multilingual Environmental Thesaurus - <https://www.eionet.europa.eu/gemet/en/about/>)

The following figures present an example of such metadata information and records in Geographic metadata extensible markup language (GMD) standard, which is an XML scheme implementation derived from ISO 19115:2003, Geographic information - Metadata completed with ISO 19115:2003/Cor.1:2006. The first figure (Figure 15) shows the full description of the temporal extent record from the INSPIRE implementing Rules for metadata (ISO19139 - <https://inspire.ec.europa.eu/id/document/tg/metadata-iso19139>) and the second (Figure 16) an example of the XML code.

IR	Reference	Part B 5.1
	Element name	Temporal extent
	Obligation / condition	Conditional: At least one temporal reference is required.
	Multiplicity	[0..*] but at least one temporal reference is required.
ISO 19115	Number	351
	Name	Extent
	Definition	Time period covered by the content of the dataset.
	XPath	identificationInfo[1]/*/*/extent/*/*/temporalElement/*/*/extent
	Data type	TM_Primitive ⁴
	Domain	As described in ISO 19108.
	Example	From 1977-03-10T11:45:30 to 2005-01-15T09:10:00
Implementing instructions		Each instance of the temporal extent may be an interval of dates or an individual date. The overall time period covered by the content of the resource may be composed of one or many instances.

Figure 15: Example of INSPIRE metadata definitions: temporal extent

```

<gmd:MD_Metadata ...
...
  <gmd:identificationInfo>
    <gmd:MD_DataIdentification>
      ...
        <gmd:extent>
          <gmd:EX_Extent>
            <gmd:temporalElement>
              <gmd:EX_TemporalExtent>
                <gmd:extent>
                  <gml:TimePeriod gml:id="IDd2feb4bb4-e66f-4ac8-ba76-8fd9bc7c8be6">
                    <gml:beginPosition>1977-03-10T11:45:30</gml:beginPosition>
                    <gml:endPosition>2005-01-15T09:10:00</gml:endPosition>
                  </gml:TimePeriod>
                </gmd:extent>
              </gmd:EX_TemporalExtent>
            </gmd:temporalElement>
          </gmd:EX_Extent>
        </gmd:extent>
      ...
    </gmd:MD_DataIdentification>
  ...
</gmd:identificationInfo>
...
</gmd:MD_Metadata>

```

Figure 16: Example of GMD metadata record

Software tools, some of them free (i.e. <https://github.com/kalxas/GIMED>), or python code (<https://gist.github.com/kalxas/e86d845f02b99067c129>) can be used to create the INSPIRE compliant metadata. Depending on the source and frequency of the stored HYPERION raw and processed data the most appropriate method for the creation of metadata (manual/automatic) can be selected.

Extracted metadata for each HYPERION product (preserved in the above described XML and raster/vector files) will be imported, stored and provided by the HYPERION Metadata Catalog, an implementation of the open source metadata catalog, GeoNetwork.

5.2 MMS product repository

The MMS product repository could be a simple FTP server, but this would not allow effective cataloguing and retrieval of the stored data. Therefore, it is proposed that the repository will incorporate a cataloguing service, with easy browsing of the stored data as well as specific APIs which could be used for the communication with HRAP. Moreover, it is desirable that this server will be based on the principles of Free and Open Source Software (FOSS) and International and Open Standards for services and protocols. Thus, our preference for the MMS repository is to use GeoNetwork.

GeoNetwork (<https://geonetwork-opensource.org/>), which is part of the OSGeo project, is a catalog application to manage spatially referenced resources. It provides powerful metadata editing and search functions as well as an interactive web map viewer. It is currently used in numerous Spatial Data Infrastructure initiatives across the world. GeoNetwork provides an easy to use web interface to search geospatial data across multiple catalogs. The search provides full-text search as well as faceted search on keywords, resource types, organizations, scale, etc. Users can easily refine the search and quickly get to the records of interest. Describe information using the online metadata editing tools. The metadata editor supports ISO19115/119/110 standards used for spatial resources and also Dublin Core format usually used for opendata portals. Using GeoNetwork, GeoSpatial layers but also services, maps or even non geographic datasets can be described in the catalog. Easily navigate across and find sources or services publishing a dataset.

GeoNetwork implements the following API protocols: OGC CSW, OAI-PMH, OpenSearch, Z39.50, and also provides its own API to interact with other systems and a DCAT/RDF search service. This is very useful for enabling communication with the HYPERION middleware and eventually with HRAP.

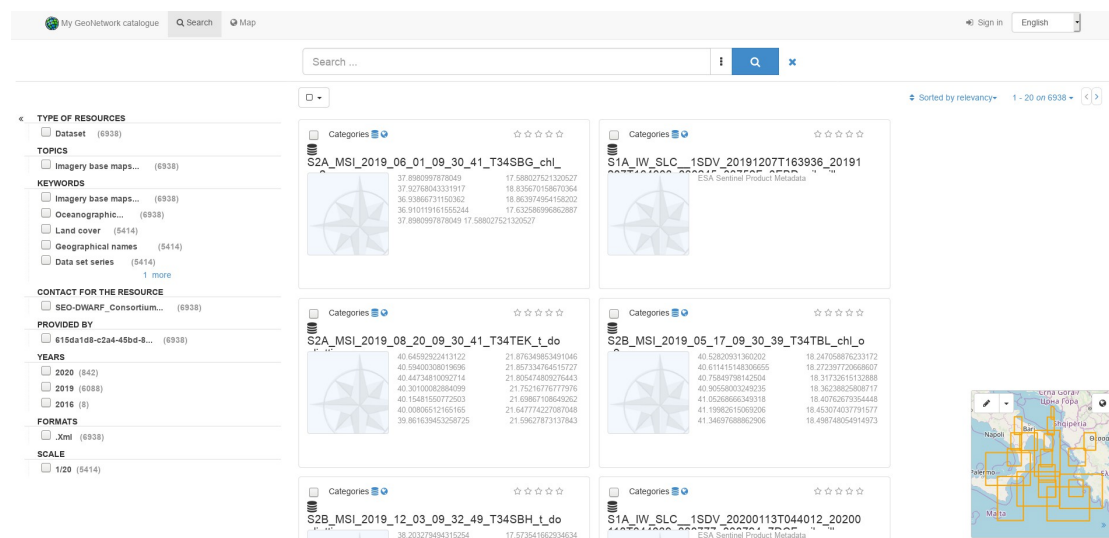


Figure 17: example browsing of data in GeoNetwork by spatial reference

The screenshot displays the 'My GeoNetwork catalogue' interface. At the top, there is a navigation bar with 'My GeoNetwork catalogue', a search bar containing 'lidar', and user information for 'admin admin (Administrator)'. Below the search bar, the results are sorted by relevancy, showing 1-19 of 19 items. On the left, there are filters for 'TYPE OF RESOURCES' (Dataset: 11, Service: 7, Series: 1), 'YEARS' (2015: 3, 2004: 1, 2002: 1), 'SPATIAL TYPES' (Grid: 3, Vector: 3), 'SERVICE TYPES' (ESRI:REST: 3, View: 1), and 'SCALE DENOMINATORS' (5000: 2, 2000: 1). The main area shows six search results, each with a thumbnail, title, and metadata. The titles are: 'Relief de la Wallonie - Modèle Numérique de Terrain (MNT) 2013-2014 -', 'Relief de la Wallonie - Modèle Numérique de Surface (MNS) 2013-2014', 'Relief de la Wallonie - Modèle Numérique de Terrain (MNT) 2013-2014', 'Relief de la Wallonie - Modèle Numérique de Surface (MNS) 2013-2014', 'Relief de la Wallonie - Modèle Numérique de Terrain (MNT) 2013-2014 -', and 'Relief de la Wallonie - Modèle Numérique de Terrain (MNT) 2013-2014 -'. All results are attributed to 'Direction de la Géométrie (SPW - SG - DGM - DGEO)'.

Figure 18: example browsing of stored data in GeoNetwork with previews

When selecting a dataset/product imported metadata will be provided in a user-friendly interface through the HYPERION MMS metadata catalog (Figure 17, Figure 18). Users can either search records by geographic region and/or other data feature(s) or browse the catalog to get a list of the available HYPERION datasets/products along with their metadata. On selecting a specific HYPERION dataset/product from the results list, its generic (INSPIRE-based) metadata description is displayed in a human readable format (Figure 19). Most common format datasets/products can also be previewed and displayed.

The screenshot shows a metadata record for a satellite image product. The title is "S2A_MSI_2019_04_25_09_40_31_T33TXF_chl_oc2". The record includes a list of coordinates, a download link, and a map showing the spatial extent of the image over a region in Italy, including cities like Foggia, Bari, and Matera. The metadata also lists keywords, language, resource identifier, legal constraints, and contact information for the user.

Figure 19: Browsing one particular product in GeoNetwork

Metadata will also be exposed by the HYPERION MMS metadata catalog in machine readable format for automated processing. In particular, the metadata catalog implements a Catalog Service for the Web (CSW) server, which provides an interface for querying and retrieving metadata records over the web. In the HYPERION context, each metadata record refers to a HYPERION product metadata set, and in particular in its generic (INSPIRE based) metadata set.

Some common CSW operations are:

- GetCapabilities: retrieves service metadata from a server
- DescribeRecord: discovers elements of the information model supported by the catalogue service. The operation allows some or all of the information model to be described.
- GetRecords: search for records, returning record IDs
- GetRecordById: retrieves the default representation of catalogue records using their identifier

Each operation is a HTTP request that when executed returns an HTTP response typically in XML format. CSW operations are combined with additional request parameter for controlling the requests and responses.

5.3 Dynamic link to hazard and resilience assessment

The self-adaptation required for HRAP involves learning from monitoring data. Physics-based deterioration models from WP4 will be integrated within a structural model implemented using *OpenSees* Finite Element (FE) software. The FE software to be used will be an open access tool enabling the desktop-, network-, or cloud-level distributed simulation of any (geo)structure under static, dynamic loads and ground deformations.

Structural models together with the data taken from the sensor input system will be fused within a stochastic embedding methodology (J. L. Beck, 2010) to produce updated degradation predictions according to the data. This will be carried out through the Bayesian Inverse Problem framework, whereby a multidimensional posterior probability density function of deterioration parameters defined in WP5 will

be obtained and the overall multi-scale structural simulation can be updated (J. L. Beck, 1998).

In Task 6.5 “Linking degradation and damage information into a dynamic hazard and resilience assessment”, a stable numerical technique for the inference of uncertain model parameters will be investigated in the context of the inverse problem. Specifically, a software toolkit will be developed for approximate Bayesian Computation (M. Chiachio et al., 2015) and model updating to integrate sensor output with Kriging-based metamodels of structures to allow rapid updating of model properties whereby hazard predictions can be made. Such computational tool will allow us dealing with the computational complexity or even intractability of the Bayesian inference for multi-scale integrity models, such as the one proposed in this research.

6. References

- Agram, P., and M. Simons, 2015. A noise model for InSAR time series, *Journal of Geophysical Research: Solid Earth*, 120(4), 2752-2771
- Bay, H., Ess, A., Tuytelaars, T., & Van Gool, L. (2008). Speeded-up robust features (SURF). *Computer vision and image understanding*, 110(3), 346-359.
- Beck J.L., Bayesian system identification based on probability logic, *Structural Control and Health Monitoring* 2010 17 (7), 825-847.
- Beck J.L., Katafygiotis L., Updating models and their uncertainties. I: Bayesian statistical framework, *Journal of Engineering Mechanics*, 1998, 124, 4, 455-461.
- Berardino, P., G. Fornaro, R. Lanari, and E. Sansosti, 2002. A new algorithm for surface deformation monitoring based on small baseline differential SAR interferograms, *Geoscience and Remote Sensing, IEEE Transactions* 1144 on, 40(11), 2375-2383
- Camps-Valls, G., L. Bruzzone, 2004. "Kernel-based methods for hyperspectral image classification", *IEEE Trans. Geosci. Remote Sens.*, vol. 43, no. 6, pp. 1351-1362, Jun. 2004.
- Camps-Valls, G., D. Tuia, L. Bruzzone, J. A. Benediktsson, 2014. "Advances in hyperspectral image classification: Earth monitoring with statistical learning methods", *IEEE Signal Process. Mag.*, vol. 31, no. 1, pp. 45-54, Jan. 2014.
- Cerra, D., Plank, S., Lysandrou, V., & Tian, J. (2016). Cultural heritage sites in danger —towards automatic damage detection from space. *Remote Sensing*, 8(9), 781.
- Chang, C.-I. 2013. *Hyperspectral Data Processing: Algorithm Design and Analysis*, Hoboken, NJ, USA:Wiley.
- Chiachio M., Beck J.L., Chiachio J., Rus G., Approximate Bayesian computation by subset simulation, *SIAM Journal on Scientific Computing* 36 (3), 2015, A1339-A1358.
- Chini, M.; Bignami, C.; Stramondo, S.; Pierdicca, N. Uplift and subsidence due to the 26 December 2004 Indonesian earthquake detected by SAR data. *Int. J. Remote Sens.* 2008, 29, 3891–3910
- Chini, Marco, Ramona Pelich, Luca Pulvirenti, Nazzareno Pierdicca, Renaud Hostache, and Patrick Matgen. 2019. “Sentinel-1 InSAR Coherence to Detect Floodwater in Urban Areas: Houston and Hurricane Harvey as a Test Case.” *Remote Sensing*.

D’Addabbo, A., A. Refice, G. Pasquariello, and F. Lovergine. 2016. “SAR/Optical Data Fusion for Flood Detection.” In *International Geoscience and Remote Sensing Symposium (IGARSS)*.

Daudt, R. C., Le Saux, B., Boulch, A., & Gousseau, Y. (2018, July). Urban change detection for multispectral earth observation using convolutional neural networks. In *IGARSS 2018-2018 IEEE International Geoscience and Remote Sensing Symposium* (pp. 2115-2118). IEEE.

De Jong, K. L., & Bosman, A. S. (2019, July). Unsupervised Change Detection in Satellite Images Using Convolutional Neural Networks. In *2019 International Joint Conference on Neural Networks (IJCNN)* (pp. 1-8). IEEE.

De Zan, F., A. Parizzi, P. Prats-Iraola, and P. López-Dekker, 2014. A SAR Interferometric Model for Soil Moisture, *IEEE Transactions on Geoscience and Remote Sensing*, 52(1), 418-425

Dey, Chandrama, Xiuping Jia, and Donald Fraser. 2008. “Decision Fusion for Reliable Flood Mapping Using Remote Sensing Images.” In *Proceedings - Digital Image Computing: Techniques and Applications, DICTA 2008*.

Dong, J., Zhang, L., Liao, M., & Gong, J. (2019). Improved correction of seasonal tropospheric delay in InSAR observations for landslide deformation monitoring. *Remote Sensing of Environment*, 233, 111370.

El Amin, A. M., Liu, Q., & Wang, Y. (2016, July). Convolutional neural network features based change detection in satellite images. In *First International Workshop on Pattern Recognition* (Vol. 10011, p. 100110W). International Society for Optics and Photonics.

Everaerts, J. (2009). *NEWPLATFORMS—Unconventional Platforms (Unmanned Aircraft Systems) for Remote Sensing*. Official Publication, (56).

Fattahi, H., and F. Amelung, 2013. DEM Error Correction in InSAR Time Series, *Geoscience and Remote Sensing, IEEE Transactions on*, 51(7), 4249-4259

Ferretti, A., C. Prati, and F. Rocca, 2001. Permanent scatterers in SAR interferometry, *Geoscience and Remote Sensing, IEEE Transactions on*, 39(1), 8-20

Fielding, E.J.; Talebian, M.; Rosen, P.A.; Nazari, H.; Jackson, J.A.; Ghorashi, M.; Walker, R. Surface ruptures and building damage of the 2003 Bam, Iran, earthquake mapped by satellite synthetic aperture radar interferometric correlation. *J. Geophys. Res.* 2005, 110, B03302:1–B03302:15

Giustarini, Laura, Renaud Hostache, Dmitri Kavetski, Marco Chini, Giovanni Corato, Stefan Schlaffer, and Patrick Matgen. 2016. “Probabilistic Flood Mapping Using Synthetic Aperture Radar Data.” *IEEE Transactions on Geoscience and Remote Sensing*.

Hinton, G. E., R. R. Salakhutdinov, 2006. "Reducing the dimensionality of data with neural networks", *Science*, vol. 313, no. 5786, pp. 504-507.

Hooper, A., H. Zebker, P. Segall, and B. Kampes, 2004. A new method for measuring deformation on volcanoes and other natural terrains using InSAR persistent scatterers, *Geophysical Research Letters*, 31(23), L23611

Hostache, R., P. Matgen, and W. Wagner. 2012. "Change Detection Approaches for Flood Extent Mapping: How to Select the Most Adequate Reference Image from Online Archives?" *International Journal of Applied Earth Observation and Geoinformation*.

Johannes L. Schönberger. "Robust Methods for Accurate and Efficient 3D Modeling from Unstructured Imagery." ETH Zürich, 2018.

Kandylakis, Z., K. Karantzalos, A. Doulamis, N. Doulamis, 2016. "Multiple object tracking with background estimation in hyperspectral video sequences", *Proc. IEEE Workshop Hyperspectral Image Signal Process. Evol. Remote Sens. (WHISPERS)*, pp. 1-4, Jun. 2016.

Lauknes, T. R., H. A. Zebker, and Y. Larsen, 2011. InSAR Deformation Time Series Using an L1-Norm Small-Baseline Approach, *IEEE Transactions on Geoscience and Remote Sensing*, 49(1), 536-546

Lin, Y., Li, S., Fang, L., & Ghamisi, P. (2019). Multispectral Change Detection with Bilinear Convolutional Neural Networks. *IEEE Geoscience and Remote Sensing Letters*.

López-Quiroz, P., M.-P. Doin, F. Tupin, P. Briole, and J.-M. Nicolas, 2009. Time series analysis of Mexico City subsidence constrained by radar interferometry, *Journal of Applied Geophysics*, 69(1), 1-15

Li, Junhua, and Wenjun Chen. 2005. "A Rule-Based Method for Mapping Canada's Wetlands Using Optical, Radar and DEM Data." *International Journal of Remote Sensing*.

Li, Yu, Sandro Martinis, Marc Wieland, Stefan Schlaffer, and Ryo Natsuaki. 2019. "Urban Flood Mapping Using SAR Intensity and Interferometric Coherence via Bayesian Network Fusion." *Remote Sensing*.

Mason, David C., Ian J. Davenport, Jeffrey C. Neal, Guy J.P. Schumann, and Paul D. Bates. 2012. "Near Real-Time Flood Detection in Urban and Rural Areas Using High-Resolution Synthetic Aperture Radar Images." *IEEE Transactions on Geoscience and Remote Sensing*.

Moropoulou, A., Georgopoulos, A., Korres, E., Spyrakos, C., & Mouzakis, C. (2017). Faithful Rehabilitation. *Civil Engineering Magazine Archive*, 87(10). <https://doi.org/10.1061/ciegag.0001244>

Lowe, D. G. (2004). Distinctive image features from scale-invariant keypoints. *International journal of computer vision*, 60(2), 91-110.

Makantasis, K., K. Karantzalos, A. Doulamis, N. Doulamis, 2015a. "Deep supervised learning for hyperspectral data classification through convolutional neural networks", *Proc. IEEE Int. Geosci. Remote Sens. Symp. (IGARSS)*, pp. 4959-4962, Jul. 2015.

Makantasis, K., K. Karantzalos, A. Doulamis, K. Loupos, 2015b. "Deep learning-based man-made object detection from hyperspectral data", *Proc. Int. Symp. Vis. Comput.*, pp. 717-727, 2015.

Makantasis, K., E. Protopapadakis, A. Doulamis, N. Doulamis, C. Loupos, 2016. "Deep convolutional neural networks for efficient vision based tunnel inspection", *Proc. IEEE Int. Conf. Intell. Comput. Commun. Process. (ICCP)*, pp. 335-342, Jul. 2016.

Massonnet, D., & Feigl, K. L. (1998). Radar interferometry and its application to changes in the Earth's surface. *Reviews of geophysics*, 36(4), 441-500.

Mondini, A. C., Santangelo, M., Rocchetti, M., Rossetto, E., Manconi, A., & Monserrat, O. (2019). Sentinel-1 SAR amplitude imagery for rapid landslide detection. *Remote Sensing*, 11(7), 760.

Plank, S. (2014). Rapid damage assessment by means of multi-temporal SAR—A comprehensive review and outlook to Sentinel-1. *Remote Sensing*, 6(6), 4870-4906.

Pulvirenti, L., N. Pierdicca, M. Chini, and L. Guerriero. 2011. "An Algorithm for Operational Flood Mapping from Synthetic Aperture Radar (SAR) Data Using Fuzzy Logic." *Natural Hazards and Earth System Science*.

Pulvirenti, Luca, Marco Chini, Nazzareno Pierdicca, and Giorgio Boni. 2016. "Use of SAR Data for Detecting Floodwater in Urban and Agricultural Areas: The Role of the Interferometric Coherence." *IEEE Transactions on Geoscience and Remote Sensing*.

Schlaffer, Stefan, Marco Chini, Laura Giustarini, and Patrick Matgen. 2017. "Probabilistic Mapping of Flood-Induced Backscatter Changes in SAR Time Series." *International Journal of Applied Earth Observation and Geoinformation*.

Schönberger, Johannes & Frahm, Jan-Michael. (2016). Structure-from-Motion Revisited. 10.1109/CVPR.2016.445.

Sun, Yonghua, Xiaojuan Li, Huili Gong, Wenji Zhao, and Zhaoning Gong. 2007. "A Study on Optical and SAR Data Fusion for Extracting Flooded Area." In *International Geoscience and Remote Sensing Symposium (IGARSS)*.

Tan, X., Y. Zhang, S. Tang, J. Shao, F. Wu, Y. Zhuang, 2012. "Logistic tensor regression for classification", *Proc. Int. Conf. Intell. Sci. Intell. Data Eng.*, pp. 573-581, 2012.

Tapinaki, S., Skamantzari, M., Chliverou, R., Evgenikou, V., Konidi, A. M., Ioannatou, E., Mylonas, A., & Georgopoulos A. (2019). 3D image based geometric documentation of a medieval fortress. *International Archives of Photogrammetry, Remote Sensing and Spatial Information Science*, XLII-2/W9, 699-705. <https://doi.org/10.5194/isprs-archives-XLII-2-W9-699-2019>

Twele, A., Cao, W., Plank, S., & Martinis, S. (2016). Sentinel-1-based flood mapping: a fully automated processing chain. *International Journal of Remote Sensing*, 37(13), 2990-3004.

Tong, X., D. T. Sandwell, and B. Smith-Konter, 2013. High-resolution interseismic velocity data along the San Andreas Fault from GPS and InSAR, *Journal of Geophysical Research: Solid Earth*, 118(1), 369-389

Tough, R. J. A., D. Blacknell, and S. Quegan, 1995. A Statistical Description of Polarimetric and Interferometric Synthetic Aperture Radar Data, *Proceedings: Mathematical and Physical Sciences*, 449(1937), 567-589, 1280

Töyrä, Jessika, and Alain Pietroniro. 2005. "Towards Operational Monitoring of a Northern Wetland Using Geomatics-Based Techniques." *Remote Sensing of Environment*.

Wu, C., Chen, H., Do, B., & Zhang, L. (2019). Unsupervised Change Detection in Multi-temporal VHR Images Based on Deep Kernel PCA Convolutional Mapping Network. *arXiv preprint arXiv:1912.08628*.

Wycoff, E., Chan, T-H., Jia, K., Ma, W.-K., Ma, Y. 2013. "A non-negative sparse promoting algorithm for high resolution hyperspectral imaging", *Proc. IEEE Int. Conf. Acoust. Speech Signal Process. (ICASSP)*, pp. 1409-1413, May 2013.

Yan, Y., Doin, M. P., Lopez-Quiroz, P., Tupin, F., Fruneau, B., Pinel, V., & Trouvé, E. (2012). Mexico city subsidence measured by InSAR time series: Joint analysis using PS and SBAS approaches. *IEEE Journal of Selected Topics in Applied Earth Observations and Remote Sensing*, 5(4), 1312-1326.

Yonezawa, C.; Takeuchi, S. Detection of Urban Damage Using Interferometric SAR Decorrelation. In *Proceedings of the IEEE IGARSS, Hamburg, Germany, 28 June–2 July 1999*; pp. 925–927

Yunjun, Z., Fattahi, H., & Amelung, F. (2019). Small baseline InSAR time series analysis: Unwrapping error correction and noise reduction. *Computers & Geosciences*, 104331.

Zhou, H., L. Li, H. Zhu, 2013. "Tensor regression with applications in neuroimaging data analysis", *J. Amer. Stat. Assoc.*, vol. 108, no. 502, pp. 540-552.

Zitova, B., & Flusser, J. (2003). Image registration methods: a survey. *Image and vision computing*, 21(11), 977-1000.

